

Optimized Modulation and Coding for Dual Modulated QR Codes

Irving Barron ¹ and Gaurav Sharma ²

¹Affiliation not available

²University of Rochester

October 30, 2023

Abstract

We present optimized modulation and coding for the recently introduced dual modulated QR (DMQR) codes that extend traditional QR codes to carry additional secondary data in the orientation of elliptical dots that replace black modules in the barcode images. By dynamically adjusting the dot size, we realize gains in embedding strength for both the intensity modulation and the orientation modulation that carry the primary and secondary data, respectively. Furthermore, we develop a model for the coding channel for the secondary data that enables soft-decoding via 5G NR (new radio) codes already supported by mobile devices. The performance gains for the proposed optimized designs are characterized via theoretical analysis, simulations, and actual experiments using smartphone devices. The theoretical analysis and simulations inform our design choices for the modulation and coding, and the experiments characterize the overall improvement in performance for the optimized design over the prior unoptimized designs. Importantly, the optimized designs significantly increase usability of DMQR codes with commonly used QR code beautification that cannibalizes a portion of the barcode image area for the insertion of a logo or image. In experiments with a capture distance of 15 inches, the optimized designs increase the decoding success rates between 10% and 32% for the secondary data while also providing gains for primary data decoding at larger capture distances. When used with beautification in typical settings, the secondary message is decoded with a high success rate for the proposed optimized designs, whereas it invariably fails for the prior unoptimized designs.

Optimized Modulation and Coding for Dual Modulated QR Codes

Irving Barron and Gaurav Sharma

Abstract—We present optimized modulation and coding for the recently introduced dual modulated QR (DMQR) codes that extend traditional QR codes to carry additional secondary data in the orientation of elliptical dots that replace black modules in the barcode images. By dynamically adjusting the dot size, we realize gains in embedding strength for both the intensity modulation and the orientation modulation that carry the primary and secondary data, respectively. Furthermore, we develop a model for the coding channel for the secondary data that enables soft-decoding via 5G NR (new radio) codes already supported by mobile devices. The performance gains for the proposed optimized designs are characterized via theoretical analysis, simulations, and actual experiments using smartphone devices. The theoretical analysis and simulations inform our design choices for the modulation and coding, and the experiments characterize the overall improvement in performance for the optimized design over the prior unoptimized designs. Importantly, the optimized designs significantly increase usability of DMQR codes with commonly used QR code beautification that cannibalizes a portion of the barcode image area for the insertion of a logo or image. In experiments with a capture distance of 15 inches, the optimized designs increase the decoding success rates between 10% and 32% for the secondary data while also providing gains for primary data decoding at larger capture distances. When used with beautification in typical settings, the secondary message is decoded with a high success rate for the proposed optimized designs, whereas it invariably fails for the prior unoptimized designs.

Index Terms—2-D barcodes, orientation modulation, elliptical dots, channel modeling, 5G error correction codes.

I. INTRODUCTION

DUAL modulated QR (DMQR) codes were recently introduced in [1]. Exploiting the high resolution capture/display hardware of contemporary mobile devices, DMQR codes enhance conventional QR codes [2] to carry an additional secondary message independent of the (conventional) primary message. Specifically, in DMQR codes, the black square data-carrying modules of conventional QR codes are replaced by black oriented elliptical dots placed within the square modules, with orientations determined by the secondary message. The resulting barcodes therefore have dual modulations: the primary message is conveyed by intensity modulation of the modules, determined by whether or not they contain a black elliptical dot, and the secondary message is conveyed by orientation modulation of the dots. The intensity modulation is compatible with conventional QR codes and the primary message is therefore decodable using standard QR code readers.

The authors are with the Department of Electrical and Computer Engineering, University of Rochester, Rochester, NY 14627-0231 USA (e-mail: ibarron@ur.rochester.edu; g.sharma@ieee.org).

Several other methods have also been proposed in the existing literature for modifying a QR code to enable the communication of additional data. We highlight the techniques that are most relevant in our DMQR code context where the objective is to recover dual messages from the captured image of the code, with the primary message decodable via standard QR code readers. In the approach proposed in [3], the standard black modules of printed QR codes are replaced with high resolution texture patterns that can be used to communicate additional private data and to authenticate the original printed document carrying the QR code (versus copies). In another approach [4], a QR code is placed within another one to create a nested QR code, where, the constituent barcodes can carry independent messages that can be recovered from two images of the nested QR code (captured at slightly different distances and/or angles) with a QR code reader. Two optimally designed layers are used in a specialized physical deployment in [5], where by capturing images of the two-layer QR code from its right/left side a QR code reader can recover messages from either of the two layers.

Standard QR codes have built in error correction capability, using which, these codes can recover the embedded message even when there are errors in the data for some of the modules. In practical deployments of QR codes, the error robustness is frequently exploited for QR code beautification. In the most common beautification approach, some of the modules in the central region of the QR code are replaced by a logo, which deliberately cannibalizes data from these modules and relies on the error correction for the recovery of the embedded message. While this approach is quite popular because of its simplicity, other methods have also been explored. Halftone QR codes [6] replace some QR code modules with binary patterns that are chosen to simultaneously satisfy dual objectives: reliable decoding of the embedded data and providing a halftone approximation to a desired monochrome image. QR Images [7], on the other hand, embed a color image into a (monochrome) QR code using halftone masks to distribute pixel modifications over the image and a probabilistic model that allows control of the trade-off between the same dual objectives of decoding robustness and the perceptual match with the color image. Neither the prior DMQR code design, nor any of other techniques that augment a QR code to communicate a secondary message, take into account the impact of beautification on the robustness of the secondary message decodability. Given the extensive use of beautification, this is a significant limitation that we also seek to remedy in the present work.

In this paper, we improve upon the prior design of DMQR

codes by optimizing the modulation and the (secondary message) error correction coding used for these barcodes. Modulation is optimized by rendering the black oriented elliptical dots in DMQR codes with different sizes based on their orientation, such that each dot covers the maximum possible area of a square module without exceeding its boundaries. To optimize the error correction coding for the secondary data, we define and characterize a model for the coding channel, which enables the computation of soft detection statistics that can be better exploited by the error correction decoder. The optimized error correction coding particularly improves the decoding robustness of the secondary data in DMQR codes, facilitating their use with beautification and in other challenging scenarios.

The main contributions of this paper are:

- We propose optimized modulation and coding for DMQR codes that enhance the robustness of secondary message communication while also offering a slight improvement for primary message communication. We present analysis to characterize the gains from the optimized modulation and to inform the choice of design parameters for DMQR codes.
- The channel modeling proposed for the coding optimization aligns DMQR codes better with mobile devices compatible the 5G NR (new radio) standard [8] by enabling the use of error correction codes from the standard.
- We demonstrate that the higher decoding robustness for the secondary message enabled by our proposed optimizations radically improves the usability of DMQR codes with commonly used beautification. Whereas the secondary message decoding for prior unoptimized designs invariably fails in the presence of beautification, a high decoding success rate (100% for a capture distance of 12 in.) is seen for the proposed optimized design.

This paper is organized as follows. Section II introduces the proposed optimized modulation and coding, additionally, the performance improvement achieved by each proposed optimization is shown independently. Section III presents experiments conducted with smartphones to compare the decoding performance between DMQR codes with and without the proposed optimizations. Section IV summarizes the main findings of the paper. Additional details of the implementations, parameters, and complementary information are presented in the Appendices. Details of mathematical derivations for several equations presented in the paper are provided in the supplementary material.

II. OPTIMIZED MODULATION AND CODING

Fig. 1 provides the context for the proposed approach. DMQR codes carry both a primary message \mathbf{m}_p and a secondary message \mathbf{m}_s . Compatibility with conventional QR code decoders is maintained for the primary message embedding; the geometry of the barcode, which identifies the individual data-carrying square modules is identical to the conventional QR codes (see Fig. 1 (b) and (c)). Fig. 1 (a) depicts the encoding process for a DMQR code. To provide decoding robustness, the primary message \mathbf{m}_p and secondary message \mathbf{m}_s are independently encoded using error correction

codes to obtain the (encoded) primary data \mathbf{c}_p and (encoded) secondary data \mathbf{c}_s , which are then embedded in the DMQR code via intensity and orientation modulation, respectively. Error correction coding (ECC) and intensity modulation for the primary message/data are matched with the QR code standard [2]. Specifically, data modules that would be white in a conventional QR code carrying the primary data remain white, whereas those that would be black instead have a black elliptical dot placed within the module (on an otherwise white background) as depicted in Fig. 1 (b) and (c). The orientation of the elliptical dots within the modules is modulated according to the secondary data \mathbf{c}_s as shown in Fig. 1 (b) and (c). Fig. 1 (d) shows the process for estimating the primary and secondary messages from a captured DMQR code image $I(\chi, \zeta)$ for which synchronization¹ has already been accomplished. The light/dark intensity variations of individual modules are demodulated in the same way as in conventional QR codes, whereby decoding compatibility is maintained with conventional QR code decoders. As illustrated in the top half of Fig. 1 (d), this intensity demodulation provides an estimate $\hat{\mathbf{c}}_p$ of the primary data, from which an estimate $\hat{\mathbf{m}}_p$ of the primary message is obtained by using a decoder matched with the primary error correction code. Once the primary message has been decoded, the secondary message decoding proceeds as shown in the bottom half of Fig. 1 (d). The geometry of the barcode and the decoded primary message identify \hat{N}_{qs} (putative) elliptical dot carrying modules (spatial regions) $\{\hat{\mathcal{B}}_i\}_{i=1}^{\hat{N}_{\text{qs}}}$ within $I(\chi, \zeta)$. Orientation information is recovered from each such region, which is then used with a decoder matched with the secondary error correction code to obtain an estimate $\hat{\mathbf{m}}_s$ of the secondary message. Specifically, the prior (baseline) DMQR codes in [1] adopted image-moment based hard-decision orientation demodulation from [9], which provides demodulated secondary data $\hat{\mathbf{c}}_s$ from which $\hat{\mathbf{m}}_s$ is obtained via error correction decoding.

The present work improves upon the original DMQR code construction [1] in two aspects. First, the modulation of both the primary and secondary data is optimized within the constraints of the module geometry. Whereas identical elliptical dots with different orientations were used in [1], as shown in Fig. 1 (b), the proposed optimized modulation uses the largest possible elliptical dots of a chosen eccentricity that fit within the modules, as shown in Fig. 1 (c). This optimized modulation magnifies both the difference in intensity between the light and dark modules that carry the primary data and also the distinction between the orientation statistics used in the demodulation. Second, we also optimize the error correction for the secondary message. Whereas the original DMQR code construction [1] used convolutional codes for the secondary message with hard-decision decoding, in the approach proposed here, we introduce a suitable channel model and soft-decision decoding. Fig. 1 (d) highlights this distinction between the baseline and the proposed optimized

¹Localization, synchronization, and geometry correction are performed as part of the standard primary message decoding process for a QR code and we denote by $I(\chi, \zeta)$ the image obtained after such synchronization, where (χ, ζ) denotes a 2D orthogonal coordinate system aligned with the QR code module grid (see [1] for further details).

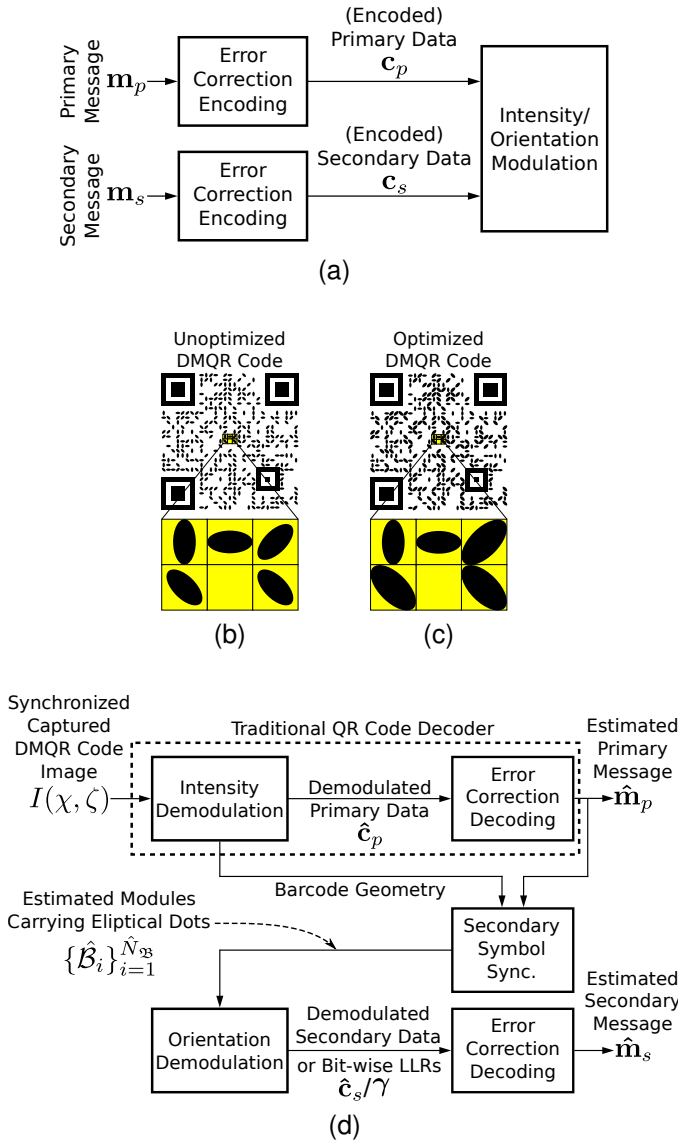


Fig. 1. DMQR code framework highlighting the differences of the proposed optimized DMQR codes with (prior) baseline designs. (a) DMQR code encoding process, (b) and (c) sample DMQR codes with unoptimized modulation [1] and the proposed optimized modulation, respectively, and (d) DMQR code decoding, where the optimized DMQR codes use bit-wise log-likelihood ratios (LLRs) with soft-decision decoding compared to the hard-decision decoding for the unoptimized designs.

DMQR codes. For the baseline DMQR codes in [1] the demodulation estimated \hat{c}_s which was then used in the binary input convolutional decoder. For the optimized DMQR code construction proposed here, the demodulation provides bit-wise log-likelihood ratios (LLRs) γ which are then utilized in more powerful soft-decision decoders. The optimization of the error correction not only improves decoding performance, but also better aligns DMQR codes with modern mobile devices by enabling the use of state of the art 5G error correction technology available in the devices.

In the remainder of the section, we provide details of the optimized modulation, the channel modeling, the bit-wise LLR computation and, using a combination of theoretical analysis and simulations, concurrently: (a) highlight the advantages

that each of these components contributes and (b) identify appropriate parameter choices for our final optimized DMQR code design which are used for the experiments in Section III.

A. Optimized Modulation

Consider the placement of an elliptical dot within its square module in the DMQR code² during the orientation modulation. Specifically, in the 2D orthogonal coordinate system (χ, ζ) for the DMQR code, consider the region $(\chi_{0_i} - \Delta/2) \leq \chi \leq (\chi_{0_i} + \Delta/2)$ and $(\zeta_{0_i} - \Delta/2) \leq \zeta \leq (\zeta_{0_i} + \Delta/2)$ corresponding to the i^{th} elliptical dot containing module \mathcal{B}_i , where $(\chi_{0_i}, \zeta_{0_i})$ denote the coordinates for the module's center and Δ the module's length along each axis. The perimeter of an elliptical dot at $(\chi_{0_i}, \zeta_{0_i})$ with its semi-major axis oriented at an angle ϕ_i with respect to the χ -coordinate can be described parametrically as $f(t) = (\chi(t), \zeta(t)), 0 \leq t \leq 2\pi$, with,

$$\chi(t) = a \cos t \cos \phi_i + b \sin t \sin \phi_i + \chi_{0_i}, \quad (1)$$

$$\zeta(t) = a \cos t \sin \phi_i - b \sin t \cos \phi_i + \zeta_{0_i}, \quad (2)$$

where a and b are the length of the semi-major and semi-minor axis, respectively. For DMQR codes, the eccentricity parameter $\epsilon = b/a$ determines the eccentricity of the elliptical dots and the orientation $\phi_i = \pi c_{s,i}/M$ is defined by the i^{th} M -ary valued secondary data symbol $c_{s,i}$ (from the M possible orientations³ $0, \pi/M, \dots, (M-1)\pi/M$). To avoid inter-module interference, the length a of the semi-major axis should be chosen so as to ensure that the elliptical dot is contained fully within its module. The horizontal and vertical modulation orientations pose the most stringent constraints on a , and based on these, the original DMQR code construction in [1] used a fixed value of $a = \Delta/2$. While this constraint ensures that the elliptical dots are contained fully within the modules, the dots for orientations other than horizontal and vertical do not extend to the module boundaries and the modulation is therefore sub-optimal for both the primary and secondary data. Larger dots would make the modules darker and better distinguishable from the white modules while also making different orientations better detectable, which benefits the primary/secondary data demodulation, respectively. To optimize the modulation, we therefore also choose a based on the modulation orientation angles. Specifically, it can be seen that (Supplementary Material Section S.II), subject to the aforementioned constraint, the largest possible length of the semi-major axis for the j^{th} modulation orientation angle $\pi j/M$, for $j = 0, 1, \dots, (M-1)$, is

$$a_j = \frac{\Delta/2}{\sqrt{\epsilon^2 \sin^2 \left(\frac{\pi j}{M} + \theta_j \right) + \cos^2 \left(\frac{\pi j}{M} + \theta_j \right)}}, \quad (3)$$

where $\theta_j = \pi/2$ for $M/4 < j < 3M/4$ and $\theta_j = 0$ otherwise. We introduce the index variable $\eta \in \{\text{U}, \text{O}\}$ to represent the unoptimized and optimized modulation scenarios, respectively,

²For the theoretical analysis, we consider idealized elliptical dots without the quantization to the discrete image grid. Subsequent simulations and experiments incorporate the quantization and other non-idealities.

³We adopt the standard convention that specified angles are measured in the counter-clockwise direction with respect to the χ axis.

and unify the notation for the semi-major axes for the two cases by defining the symbol

$$a_j^\eta \stackrel{\text{def}}{=} \begin{cases} \frac{\Delta}{2}, & \eta = \text{U} \\ a_j, & \eta = \text{O} \end{cases}. \quad (4)$$

We characterize the improvements offered by the proposed optimized modulation over the prior approach both analytically and via simulations. For the theoretical analysis, we consider an idealized infinite resolution setting where the elliptical dots correspond to elliptical disks for which: (a) areas correspond to the intensity modulation signal for the primary data and (b) area moments of inertia [10] correspond to the image moments used for detection of the secondary data, both of which can be computed in closed form.

The area of the elliptical disks constitutes the intensity modulation signal for the primary data. An elliptical disk with semi-major axis a_j^η and eccentricity parameter ϵ has an area $\pi\epsilon (a_j^\eta)^2$. The average value,

$$\begin{aligned} \mathcal{G}_p(M) &= \frac{1}{M} \sum_{j=0}^{M-1} \frac{\pi\epsilon (a_j^{\text{O}})^2}{\pi\epsilon (a_j^{\text{U}})^2} \\ &= \frac{1}{M} \sum_{j=0}^{M-1} \frac{1}{\epsilon^2 \sin^2\left(\frac{\pi j}{M} + \theta_j\right) + \cos^2\left(\frac{\pi j}{M} + \theta_j\right)}, \end{aligned} \quad (5)$$

of the ratio of the areas for the optimized and unoptimized cases therefore represents the ‘‘SNR gain’’ for the primary data modulation. Fig. 2 (a) shows a plot of the gain $\mathcal{G}_p(M)$ as a function of the number $\log_2(M)$ of bits-per-symbol for different values of ϵ , where it can be seen that $\mathcal{G}_p(M) \geq 1$. For most values of ϵ and M , there is always a benefit when optimized modulation is used, and the highest $\mathcal{G}_p(M)$ for each value of ϵ occurs when $\log_2(M) = 2$. Note that, if $\epsilon = 1$ or $\log_2(M) = 1$, then $\mathcal{G}_p(M) = 1$, which is expected. Specifically, for $\epsilon = 1$, the elliptical dots with/without optimal modulation turn into circles, while, for $\log_2(M) = 1$, the elliptical dots in both modulation approaches are identical (limited by the horizontal/vertical boundaries of the square modules).

Next, we develop a modulation constellation representation in terms of the area moments of inertia of the orientation-modulated elliptical disks, which enables a comparison of the proposed optimized secondary data modulation against the unoptimized modulation using a standard digital communication methodology [11, Chap. 4]. In this process, we also introduce an advantageous normalization that eliminates dependence of the area moments of inertia on the module size (i.e., image resolution). Specifically, consider a module with an elliptical dot with modulation orientation angle $\pi j/M$. Using an elliptical disk representation for the dot, the square-root of the normalized area moment of inertia over the module about an axis through the center at an orientation angle $\pi k/M$ is (Supplementary Material Section S.III)

$$\sqrt{\frac{\tau_{j,k}^\eta}{\pi\epsilon (a_j^\eta)^2 \Delta^2}} = \frac{a_j^\eta}{2\Delta} \sqrt{\cos^2 \psi_{j,k} + \epsilon^2 \sin^2 \psi_{j,k}}, \quad (6)$$

where $\psi_{j,k} = \pi(k - j)/M$, $\tau_{j,k}^\eta$ denotes the area moment of inertia along the k^{th} modulation orientation for $k = 0, 1, \dots, (M - 1)$.

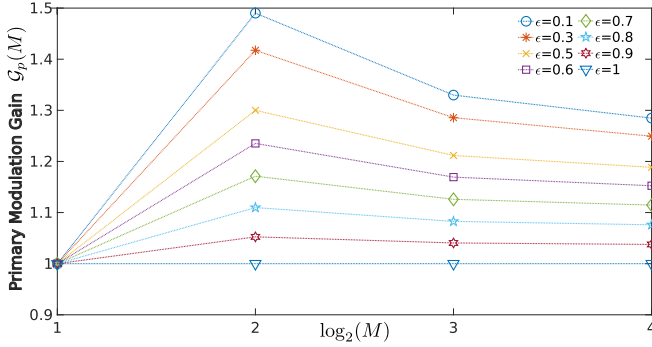
The values of the normalized area moments define the constellation points for the secondary modulation, in terms of which we can compare the proposed optimized modulation against the unoptimized version. Under a high SNR assumption where the errors due to nearest neighbors in the constellation dominate, the SNR gain for the optimized modulation over the unoptimized modulation (for the secondary data) can be quantified as the average of the ratios of the distances to the nearest neighbor in the area moment of inertia space for the two cases, which is obtained as

$$\mathcal{G}_s(M) = \frac{1}{M} \sum_{j=0}^{M-1} \frac{\sqrt{\frac{\tau_{j,j}^{\text{O}}}{\pi\epsilon (a_j^{\text{O}})^2 \Delta^2}} - \sqrt{\frac{\tau_{j,n_j}^{\text{O}}}{\pi\epsilon (a_j^{\text{O}})^2 \Delta^2}}}{\sqrt{\frac{\tau_{j,j}^{\text{U}}}{\pi\epsilon (a_j^{\text{U}})^2 \Delta^2}} - \sqrt{\frac{\tau_{j,n_j}^{\text{U}}}{\pi\epsilon (a_j^{\text{U}})^2 \Delta^2}}}, \quad (7)$$

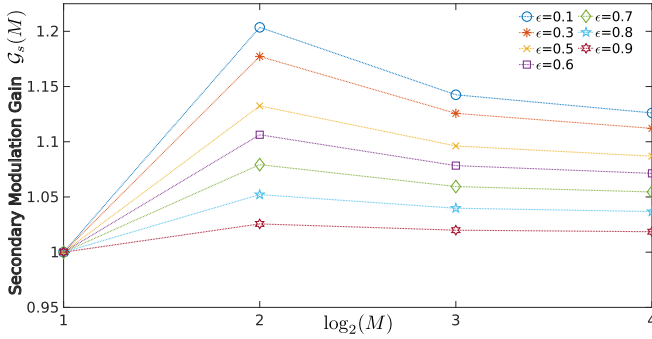
where n_j denotes the nearest neighbor for the j^{th} area moment of inertia. Fig. 2 (b) depicts the gain factor $\mathcal{G}_s(M)$ as a function of the number $\log_2(M)$ of bits-per-symbol for different values of ϵ . Optimized modulation always benefits the secondary data except for binary orientation modulation ($\log_2(M) = 1$) for which $\mathcal{G}_s(M) = 1$. Once again the highest gain occurs when $\log_2(M) = 2$. Note that, $\epsilon = 1$ is omitted because it corresponds to the case of exactly circular dots, which cannot convey information through their orientation.

To further demonstrate the benefit of the proposed optimized modulation and to gain insight for parameter choices, we perform simulations via ISETCam [12], which enables realistic simulations of display/capture systems and was also used and validated in prior work [1]. For the simulations and subsequent experiments, we focused on the 4-ary modulation scenario because it was shown to be the most effective operating point for unoptimized modulation in [1] and because the theoretical analysis also indicates the largest performance gains for the optimized modulation for $M = 4$. DMQR codes with baseline/optimized modulation were created by using $\epsilon = 0.1, 0.2, \dots, 0.9$, and 4-ary orientation modulation. Display renderings and camera captures of the DMQR codes were then simulated for capture distances $D \in \{9, 12, 15, 18\}$ inches using display/camera resolutions typical in current entry-level smartphones, which represent the most challenging use cases because of their lower spatial resolutions compared with higher-end smartphones. Further details of the simulations are included in Appendix A.

To characterize the demodulation performance, bit error rates (BERs) were computed for estimates of the primary data obtained by using a conventional QR code decoder, and for estimates of the secondary data obtained by using the image-moment based hard-decision detector proposed for the baseline DMQR code [1]. Fig. 3 presents the BER for the primary and secondary data and compares these for the unoptimized (baseline) and optimized modulation as a function of the eccentricity parameter ϵ and capture distance D ; contours corresponding to several BER values ranging between 10^{-3} and 0.3 are shown in the figure. These BER estimates are each



(a) Primary (intensity) modulation



(b) Secondary (orientation) modulation

Fig. 2. SNR gains, (a) $\mathcal{G}_p(M)$ for primary and (b) $\mathcal{G}_s(M)$ for secondary data realized by using the proposed optimized modulation compared with the unoptimized modulation, as a function of the number $\log_2(M)$ of bits-per-symbol and the eccentricity parameter ϵ . The plots highlight the benefit of the proposed optimized modulation for both primary and secondary data modulation.

obtained from 400 Monte-Carlo simulations of DMQR code display and capture which represent 2.24×10^5 primary bits and 2.64×10^5 secondary bits ($\equiv 1.32 \times 10^5$ 4-ary secondary symbols). The comparison in Fig. 3 reiterates the findings from [1] that the eccentricity parameter ϵ mediates a trade-off between the robustness of primary and secondary data modulation. Furthermore, in the vicinity of $\epsilon = 0.5$ (see horizontal dashed gray line in Fig. 3), the optimized modulation offers a significant improvement over the unoptimized modulation for both the primary and secondary data, particularly in the BER range between 10^{-3} and 0.1, which is of operational interest for typical error correction coding.

B. Optimized Secondary Message ECC

As indicated earlier, to optimize secondary message decoding⁴, we use state of the art error correction codes from the 5G NR standard. These codes work with soft detection statistics, specifically bit-wise LLRs, which we compute using a statistical model of the coding channel for the secondary data. We motivate and develop this model next. From two-dimensional mechanics, it is known [10] that area moments of inertia along two orthogonal directions combined with a

⁴To ensure compatibility with conventional QR code decoders, error correction coding for the primary message in DMQR codes adheres to the QR code standard [2].

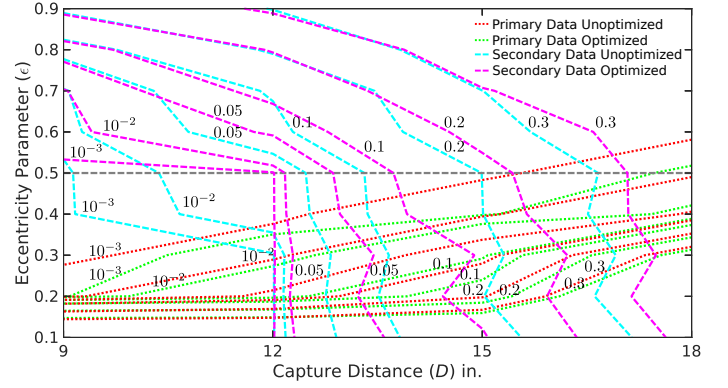


Fig. 3. BER contours for primary and secondary data as a function of the eccentricity parameter ϵ and capture distance D for the proposed optimized modulation (green/magenta) and for unoptimized modulation (red/cyan).

corresponding product of inertia are sufficient for computing the area moment of inertia about any orientation (see Appendix B for a summary). For detecting the orientation of a putative elliptical dot within an estimated module region $\hat{\mathcal{B}}$, we therefore use, as detection statistics, the image moments r_χ , r_ζ computed along the χ and ζ axes, and the corresponding product of inertia $r_{\chi\zeta}$, where these are computed as

$$r_\chi = \frac{\sum_{\chi, \zeta \in \hat{\mathcal{B}}} \bar{I}(\chi, \zeta) (\chi - \bar{\chi})^2}{\sum_{\chi, \zeta \in \hat{\mathcal{B}}} \bar{I}(\chi, \zeta)}, \quad (8)$$

$$r_\zeta = \frac{\sum_{\chi, \zeta \in \hat{\mathcal{B}}} \bar{I}(\chi, \zeta) (\zeta - \bar{\zeta})^2}{\sum_{\chi, \zeta \in \hat{\mathcal{B}}} \bar{I}(\chi, \zeta)}, \quad (9)$$

$$r_{\chi\zeta} = \frac{\sum_{\chi, \zeta \in \hat{\mathcal{B}}} \bar{I}(\chi, \zeta) (\chi - \bar{\chi})(\zeta - \bar{\zeta})}{\sum_{\chi, \zeta \in \hat{\mathcal{B}}} \bar{I}(\chi, \zeta)}, \quad (10)$$

with $\bar{I}(\chi, \zeta)$ denoting the image obtained by binarizing $I(\chi, \zeta)$, and

$$\bar{\chi} = \frac{\sum_{\chi, \zeta \in \hat{\mathcal{B}}} \bar{I}(\chi, \zeta) \chi}{\sum_{\chi, \zeta \in \hat{\mathcal{B}}} \bar{I}(\chi, \zeta)}, \quad (11)$$

denoting the χ coordinate of the center of mass (COM) of the estimated module $\hat{\mathcal{B}}$, and $\bar{\zeta}$ as the COM ζ coordinate, which is similarly obtained. The probabilistic model of the channel is then represented as a conditional probability density function $f_{\mathbf{r}}(\mathbf{r}|\phi_j)$ for the detection statistics $\mathbf{r} = [r_\chi, r_\zeta, r_{\chi\zeta}]$ under the assumption that the orientation ϕ_j was used for the dot in the module.

Assuming conditional independence⁵, the channel model becomes

$$f_{\mathbf{r}}(\mathbf{r}|\phi_j) = f_{r_\chi}(r_\chi|\phi_j) f_{r_\zeta}(r_\zeta|\phi_j) f_{r_{\chi\zeta}}(r_{\chi\zeta}|\phi_j). \quad (12)$$

The proposed channel model is then specified by the marginal conditional densities $f_{r_\chi}(r_\chi|\phi_j)$, $f_{r_\zeta}(r_\zeta|\phi_j)$ and $f_{r_{\chi\zeta}}(r_{\chi\zeta}|\phi_j)$. To keep the channel modeling task tractable, we use an exponential power density family parametric approximation for

⁵The assumption was empirically validated on experimental data, as summarized in Appendix C.

the marginal conditional densities, which take the functional form [13]

$$f_Y(y) = \frac{1}{2\alpha\Gamma\left(1 + \frac{1}{\beta}\right)} \exp\left(-\left|\frac{y - \mu}{\alpha}\right|^\beta\right), \quad (13)$$

where $\Gamma(\cdot)$ is the gamma function, α , β and μ correspond to the scale, shape and mean parameters. For $\beta = 1$ and $\beta = 2$, the expression in (13) becomes the Laplacian and Gaussian distribution, respectively. Based on empirical evaluation, the shape parameter was set to $\beta = 1$. The scale and mean parameters are estimated using an expectation maximization [14] like procedure (see Appendix E for details).

The complete set of LLRs γ for the secondary encoded data is obtained by using the channel model to compute LLRs on a module-by-module basis. Specifically, $\gamma = (\mathbf{g}_1, \mathbf{g}_2, \dots, \mathbf{g}_{\hat{N}_{\mathfrak{B}}})$ where $\mathbf{g}_i = (g_{i0}, g_{i1}, \dots, g_{i(\log_2(M)-1)})$ is the vector of $\log_2(M)$ bit-wise LLRs corresponding to the i^{th} module, computed for $i = 1, 2, \dots, \hat{N}_{\mathfrak{B}}$ and $l = 0, 1, \dots, \log_2(M) - 1$ as

$$\begin{aligned} g_{il} &= \ln\left(\frac{f_{\mathbf{b}}(b_l = 1|\mathbf{r})}{f_{\mathbf{b}}(b_l = 0|\mathbf{r})}\right) = \ln\left(\frac{\sum_{\mathbf{b}:b_l=1} f_{\mathbf{b}}(\mathbf{b}|\mathbf{r})}{\sum_{\mathbf{b}:b_l=0} f_{\mathbf{b}}(\mathbf{b}|\mathbf{r})}\right) \\ &= \ln\left(\frac{\sum_{\mathbf{b}:b_l=1} f_{\mathbf{r}}(\mathbf{r}|\mathbf{b})}{\sum_{\mathbf{b}:b_l=0} f_{\mathbf{r}}(\mathbf{r}|\mathbf{b})}\right) \\ &\equiv \ln\left(\frac{\sum_{\mathbf{b}:b_l=1} f_{\mathbf{r}}(\mathbf{r}|\phi_{\mathbf{b}})}{\sum_{\mathbf{b}:b_l=0} f_{\mathbf{r}}(\mathbf{r}|\phi_{\mathbf{b}})}\right), \end{aligned} \quad (14)$$

where \mathbf{b} is a vector of bits that represents the M -ary symbol for the i^{th} elliptical dot module, and b_l denotes the l^{th} bit of \mathbf{b} .

To select between LDPC and polar codes from the 5G NR standard, we assess the relative performance of these error correction codes for our typical application setting, with a message length of 320 bits and a coding channel facsimile obtained by re-using our modulation simulations of Section II-A. Specifically, for each D and ϵ the channel is modeled by a stochastic look-up table indexed by M -ary symbols \mathbf{b} (equivalently, by the corresponding modulation orientation $\phi_{\mathbf{b}}$) that outputs a random sample from the detection statistics observed in the modulation simulation for that modulation orientation. Randomly generated messages were encoded independently with the 5G NR standard polar/LDPC codes⁶ and detection statistics corresponding to the communication of corresponding modulated symbols were obtained using our aforementioned simulated modulation channel. Bit-wise LLRs were then computed from these detection statistics, as previously described, which were then used in the corresponding decoder. The performance of the codes was compared by computing the decoding success rate (DSR), i.e., the percentage of received encoded messages that decode successfully after error correction. Across different choices of capture distances and eccentricity parameter values ϵ in the reasonable (see Fig. 3) range $[0.3, 0.7]$, the 5G polar codes consistently offered a better performance than the 5G LDPC codes. Specifically, either both codes had a DSR of 100% or

⁶Parameter choices and implementation details are available in Appendix D.

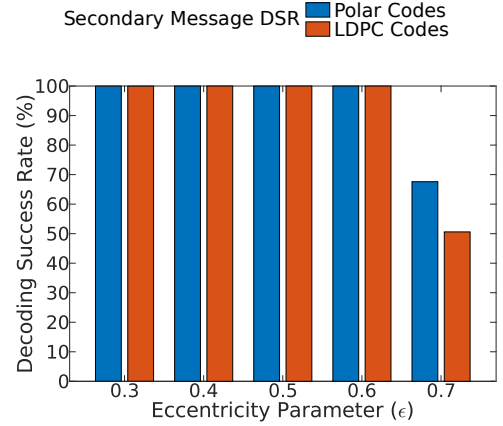


Fig. 4. Comparison of (percent) DSRs for secondary message recovery for 5G polar and LDPC codes as a function of the eccentricity parameter ϵ obtained for a capture distance $D = 12$ in.

0% or the polar codes had a higher DSR. A sample result over 10^5 simulations is shown in Fig. 4 for a typical barcode capture distance $D = 12$ in. and $\epsilon \in \{0.3, 0.4, \dots, 0.7\}$, where the performance advantage of the polar codes can be seen, an advantage that was validated for different distances and eccentricity values in additional simulations. Hence, for the final optimized DMQR code design, we use 5G polar codes to encode/decode the secondary message.

III. EXPERIMENTS AND RESULTS

To assess the benefit of the proposed optimizations in a real-world setting, we conducted experiments using smartphones for the display and capture of DMQR codes. We evaluated and compared the performance of the proposed optimized DMQR codes against the baseline DMQR codes presented in our prior work [1]. The baseline DMQR codes do not incorporate the optimizations for the modulation and coding proposed here; specifically, the orientation modulation uses fixed size elliptical dots, and convolutional codes with hard-decision decoding are used for error correction. In contrast, the proposed optimized DMQR codes use the maximal dot size allowable based on the modulation orientation (as outlined in Section II-A) and polar codes with soft-decision decoding (as described in Section II-B). Our experiments explored and compared the performance for the optimized and baseline DMQR codes in two scenarios that are both of practical interest: (a) when the barcodes are used in their unabridged format and (b) when the barcodes are used with beautification, where a part of the area dedicated to the barcode is deliberately cannibalized for insertion of a logo or image. We report on each of these in turn below.

For our physical experiments, we chose smartphones whose display and camera resolution specifications resemble current entry-level devices, which represent the most challenging situation for DMQR codes because of our reliance on spatial detail for secondary data communication. Specifically, we used (Samsung Galaxy) Nexus and (Samsung Galaxy) J3 smartphones whose display, capture, and compression related specifications are listed in Table I. Based on the results in

TABLE I
RELEVANT SPECIFICATIONS OF MOBILE DEVICES

Device	Camera Resolution (Pixels)	JPEG Quality Factor	Display Resolution (Pixels/Inch)
Nexus	2592 × 1944	95	316
J3	2576 × 1932	97	294

Section II, we set $\epsilon = 0.5$, $M = 4$ and created optimized and baseline DMQR codes carrying identical primary and secondary messages corresponding, respectively, to a URL and a generated secure password string (See Appendix E for details). Each of the barcodes was displayed on one smartphone and 100 images of the barcode image were captured on the other smartphone for each of the capture distances $D \in \{15, 18, 21\}$ in.. The process was then repeated after interchanging the display and capture devices. Images were captured with an approximate fronto-parallel geometry that is typically used for QR code capture, though the geometry was not strongly controlled. Decoding was attempted for the primary and secondary messages on each captured image and, to quantify the performance, the DSRs for the primary and secondary messages were computed and compared for each capture distance for the proposed optimized DMQR code and the baseline DMQR code.

DSRs for the (proposed) optimized and for the baseline DMQR codes are shown and compared in Fig. 5 for the two devices for capture distances D of 15, 18, and 21 in., where the blue and orange bar colors correspond, respectively, to the optimized and baseline designs with the homogeneous color and cross-hatched patterns indicating the Nexus and J3 capture devices, respectively. Figures 5 (a) and (b) present the DSR for the secondary and primary messages, respectively. For the secondary message, which is the key focus of our optimizations, the optimized DMQR code consistently demonstrates a higher DSR than the prior baseline design across all three capture distances. The gains in DSR are largest for the 18 in. capture distance, where the DSR for optimized DMQR codes are higher by 67% and 66% for the Nexus and J3, respectively. The average improvement in DSR is 21%, 66.5% and 2.5% for $D = 15, 18$ and 21 in., respectively, although as expected and illustrated in Fig. 5 (a), there is significant variation across the two devices due to the differences in their spatial resolutions. For the primary message, for capture distances up to 18 in., both the optimized and baseline DMQR codes have a 100% DSR for both devices, whereas at a capture distance of $D = 21$ in., the optimized DMQR code exhibits a DSR that is higher than the baseline by 32% on the Nexus and 10% on the J3. Overall, the results highlight the significant improvement offered by the proposed optimized DMQR codes.

In practical applications using QR codes on mobile devices, it is very common to beautify the barcode by replacing a part of the QR code with an image or logo. Examples of such beautification are shown in Fig. 6 (a) and (b) using the baseline and optimized DMQR code designs, respectively. The process deliberately sacrifices the data embedded in the DMQR code modules that were originally located in the area consumed by the image/logo and relies on the error correction coding

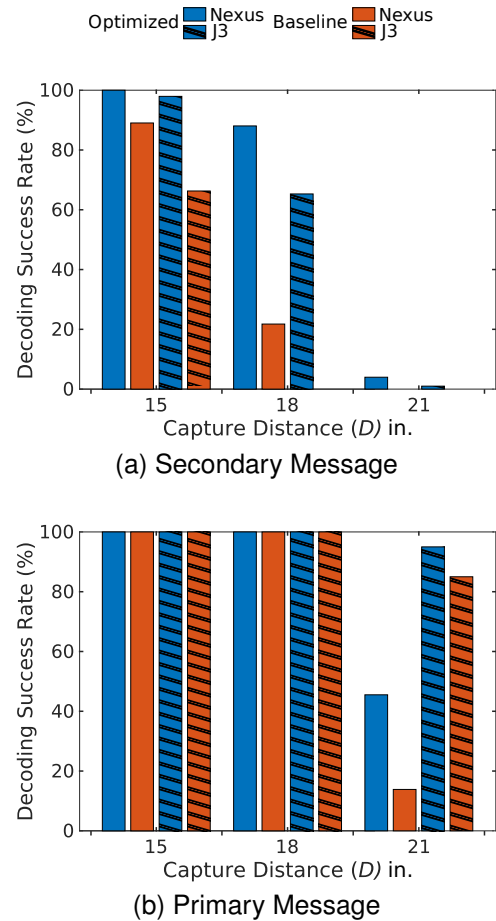


Fig. 5. Comparison of (percent) DSRs for the proposed optimized (blue) vs baseline (orange) DMQR codes as a function of the capture distance $D = 15, 18, 21$ inches computed from experiments with physical mobile devices for capture/display for: (a) secondary message and (b) primary message.

for recovery of the embedded messages. A key motivation for optimizing the modulation and coding for DMQR codes is to create additional headroom for the beautification by supporting recovery despite higher per-module error rates, particularly for the secondary message embedded via orientation modulation. We therefore also conducted experiments to characterize and compare the decoding performance for beautified versions of optimized and unoptimized DMQR codes. The set-up for these experiments was identical to that described earlier in this section, except that we used beautified versions of the optimized/baseline DMQR codes where a logo covered the center region replacing approx 12% of the data carrying modules, of which, roughly half would carry secondary data. Secondary and primary message DSRs for beautified versions of the optimized and baseline DMQR codes are shown and compared in Fig. 7 for the two devices for capture distances D of 12, 15 and 18 in., where we use the same convention for the bar plot colors and patterns as Fig. 5. The barplots in Fig. 7 (a) clearly highlight the benefit that the optimized modulation and coding offer for the recovery of the secondary message in the presence of beautification. For the baseline (unoptimized) DMQR codes, the secondary message recovery failed across all devices and capture distances (the 0% DSR bars corresponding to these cases in Fig. 7 (a) are completely

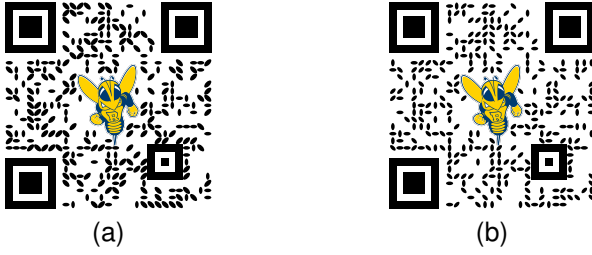
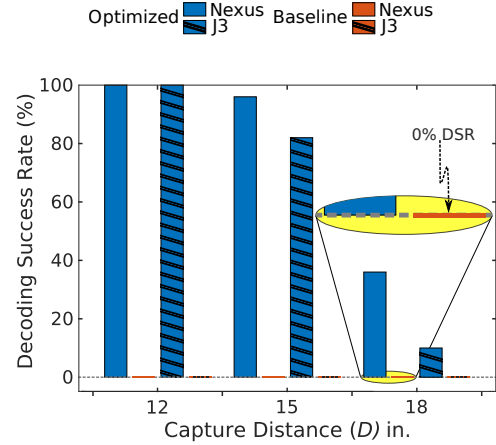


Fig. 6. Examples of beautified DMQR codes: (a) optimized and (b) baseline. To be visually appealing, some (center region) modules from the DMQR codes have been deliberately cannibalized to add a logo.

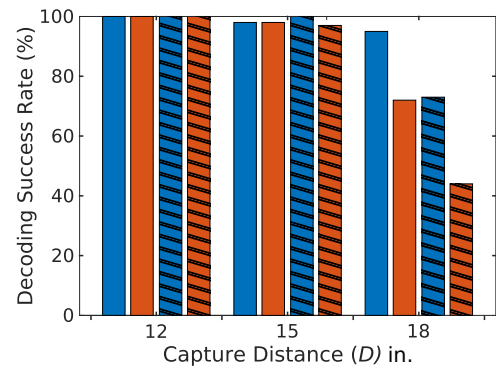
coincident with the abscissa), whereas for the optimized DMQR codes proposed here, high DSRs (average values of 100% and 89%, respectively) are observed for capture distances of $D = 12$ and 15 in. and, even at a capture distance of $D = 18$ in., a 23% average DSR is attained. We note that the gains in secondary message DSR in the presence of beautification can be principally attributed to the optimized error correction coding using the soft-decision LLRs. For modules cannibalized by the beautification, the soft-decision LLRs are often close to 0, signaling erasure of these symbols, whereas under the hard-decision decoding in the baseline unoptimized DMQR codes, a choice between the alternative modulation orientations is forced that fails to convey to the error correction decoder that these modules have essentially been erased by the beautification. Fig. 7 (a) also highlights the variation in performance across devices, which was also noted earlier in Fig. 5. DSRs for the primary message from the experiment with beautified DMQR codes are shown in the bar plots in Fig. 7 (b), match the 100% DSR for the secondary message at $D = 12$ in. and exceed the secondary message DSR for larger distances. Overall, these results indicate that the optimized DMQR codes significantly improve the recovery of the secondary message from the beautified optimized DMQR codes and thereby also improve the usability of DMQR codes with commonly-used beautification.

IV. CONCLUSION

The optimized DMQR codes proposed here provide significant performance gains over the prior baseline (unoptimized) designs. Large improvements in DSRs are seen for secondary message recovery, which benefits from both the optimizations of the modulation and the error correction coding and, simultaneously, minor improvements in DSRs are also seen for the primary message from the modulation optimization. Specifically, the proposed channel modeling for the secondary modulation enables the use of state of the art error correction codes from the 5G NR standard, for which implementation support is already built into modern mobile devices, and which make the secondary message recovery much more robust in comparison with the baseline DMQR codes. Importantly, the improved robustness of secondary message recovery for the optimized DMQR codes significantly improves their usability with standard QR code beautification, where a region of the codes spatial support is replaced by a logo cannibalizing the data it would otherwise carry. In our experiments with



(a) Secondary Message



(b) Primary Message

Fig. 7. Comparison of (percent) DSRs obtained with beautified versions of the proposed optimized (blue) vs baseline (orange) DMQR codes as a function of the capture distance $D = 12, 15, 18$ inches computed from experiments with physical mobile devices for capture/display for: (a) secondary message and (b) primary message.

beautified DMQR codes, DSRs of 100% and above 82% were observed for captured distances of 12 and 15 in., respectively, with the optimized designs proposed here, whereas the baseline DMQR codes failed to decode (0% DSR).

V. ACKNOWLEDGMENT

We thank the Center for Integrated Research Computing, University of Rochester, for providing access to computational resources for this work.

APPENDIX A

ISSET SIMULATION CONFIGURATION AND PARAMETERS

In Section II-A (specifically for Fig. 3), simulations were used to compare the relative performance of the proposed optimized modulation against the prior baseline (unoptimized) modulation across a range of design parameter choices and operating conditions. DMQR code images spanning the design configuration space, i.e., with/without optimized modulation and alternative values of the eccentricity parameter ϵ , were generated with a URL as the primary data and randomly generated secondary data. Specifically, we used the URL <https://labsites.rochester.edu/gsharma/> as the primary message

which resulted in a QR code with $29 \times 29 = 841$ modules for which 330 of the data-carrying modules were black (dark), which were replaced in the DMQR codes by elliptical dot modules, where the orientation of the dots was chosen from one of the four orientations for 4-ary modulation ($M = 4$) based on the randomly generated secondary data. A module of $\Delta = 11$ pixels was used, resulting in a size of 319×319 pixels for the rendered DMQR code. A white uniform border was added to aid synchronization (as in prior work [1], [15]), which increased the size to 415×415 pixels. The display and capture of these images was simulated using the ISETCam software toolkit [12], [16] with a display model having pixel density of 326 pixels per inch (PPI) (a screen option in the toolkit corresponding to an Apple LCD monitor) and a camera with a sensor resolution of 1920×1080 pixels. Settings of capture noise were kept at the default values in ISETCam. The impact of image compression, which is frequently integrated within camera capture pipelines, was included in the simulations by saving the simulated captured images as JPEG files with a quality factor of 97.

APPENDIX B

IMAGE MOMENT ABOUT A ROTATED AXIS

Our choice of detection statistics $r_\chi, r_\zeta, r_{\chi\zeta}$ in Section II-B was motivated by the key property in two-dimensional mechanics that area moments of inertia for a planar structure about any axis of rotation can be computed in terms of area moments of inertia about two orthogonal axes and a corresponding product of inertia [10, Appendix A]. The same property also applies directly to image moments: the image moment r_θ about an axis passing through the origin at any angle θ (counter-clockwise) with respect to the χ -axis can be obtained in terms of the the image moments r_χ, r_ζ along the χ and ζ axes, and the corresponding product of inertia $r_{\chi\zeta}$, which were defined in (8)–(10). Specifically,

$$\begin{aligned} r_\theta &\stackrel{\text{def}}{=} \frac{\sum_{\chi, \zeta \in \hat{\mathcal{B}}} \bar{I}(\chi, \zeta) (x_\theta - \bar{x}_\theta)^2}{\sum_{\chi, \zeta \in \hat{\mathcal{B}}} \bar{I}(\chi, \zeta)} \\ &= \frac{r_\chi + r_\zeta}{2} - \frac{r_\zeta - r_\chi}{2} \cos 2\theta + r_{\chi\zeta} \sin 2\theta, \end{aligned} \quad (15)$$

where $x_\theta = \chi \cos \theta + \zeta \sin \theta$ and

$$\bar{x}_\theta = \frac{\sum_{\chi, \zeta \in \hat{\mathcal{B}}} \bar{I}(\chi, \zeta) \chi \theta}{\sum_{\chi, \zeta \in \hat{\mathcal{B}}} \bar{I}(\chi, \zeta)}. \quad (16)$$

APPENDIX C

DETECTION STATISTICS CONDITIONAL INDEPENDENCE VALIDATION

We empirically validated that the 3×3 covariance matrices $\{\mathbf{K}_i\}_{i=1}^P$ of detection statistics \mathbf{r} conditioned on ϕ_j for $j = 0, 1, 2, 3$ are close to diagonal, and therefore the conditional independence of the detection statistics in the channel model of Section II-B is reasonable. Specifically, as in [17], we quantify how close empirically evaluated covariance matrices are to diagonal by computing the fraction of the energy concentrated in the diagonal terms, which is expressed in the decibel scale as $10 \log_{10} (\sum_i \|\text{diag}(\mathbf{K}_i)\|_F^2 / \sum_i \|\mathbf{K}_i\|_F^2)$,

where $\|\mathbf{A}\|_F$ denotes the Frobenius norm of the matrix \mathbf{A} and $\text{diag}(\mathbf{A})$ denotes a diagonal matrix with diagonal entries identical to those in \mathbf{A} . When \mathbf{K}_i is a diagonal matrix this measure has an ideal value of 0 dB and values in the vicinity of 0 indicate a close to diagonal matrix, which was the case for empirically observed covariance matrices for the data from our experiments of Section III. For example, for a capture distance of $D = 15$ in., the aforementioned measure of diagonal dominance had values of $-0.001, -1.145, -0.002, -1.032$ dB for $j = 0, 1, 2, 3$, respectively.

APPENDIX D

POLAR AND LDPC CODE PARAMETERS

The experiments in Section II-B compared polar and LDPC codes from the 5G NR standard [8] and based on the results presented there, polar codes were chosen and used for the experiments in Section III. Based on our application setting, a block length of $n = 660$ bits and $k = 320$ message bits was used for both codes. In both cases a 16 bit CRC was also used, which was used to validate the decoded message for the LDPC code and for CRC-aided decoding for the polar code. Specifically, for the decoding of the polar code, the CRC-aided successive cancellation-list algorithm [18] was used for which a list size $L = 32$ was chosen as in [19]. Puncturing was used for achieving rate compatibility as per [20] where the frozen bits were generated to comply with the standard. Encoding and decoding was implemented for the LDPC codes using MATLABTM and for polar codes using the AFF3CT toolbox [19], [21].

APPENDIX E

IMPLEMENTATION DETAILS FOR SMARTPHONE-BASED EXPERIMENTS

The experiments with physical smartphones in Section III compared the DSRs for the proposed optimized and for the baseline (unoptimized) design. Both barcodes used the URL <https://labsites.rochester.edu/gsharma/> as the primary message (same as in Appendix A), which was protected by level M error correction specified in the QR code standard [2], i.e., by a Reed-Solomon code that can compensate for an approximately 15% BER. The secondary message was set as the 320 bit long secure password `g5r{GRw}^Gu*kk^c:Q)s/:Sys7q?cgvA5rCM:!s% that was generated via an online strong password generator [22] and error correction for the secondary message used convolutional codes [23] for the baseline DMQR code as described in [1] and polar codes for the optimized DMQR code as described in Appendix D. Versions of the optimized and baseline DMQR codes, created by placing a logo in the center that replaced the modules, were used for the experiments with beautified codes. The logo overlapped 66 modules, specifically, 28 white and 38 (black) elliptical dot modules. The ZXing [24], open source QR code decoder was used to recover synchronization information, to obtain the demodulated primary data $\hat{\mathbf{c}}_p$ for the computation of (primary) modulation BERs, and to estimate the primary message $\hat{\mathbf{m}}_p$ using the standard QR code decoding. The secondary message decoding for the baseline`

DMQR codes followed [1] with hard-decision demodulation followed by Viterbi decoding. The secondary message (polar) decoder for the optimized DMQR code, used bit-wise LLRs γ obtained using (14), where the marginal conditional densities $f_{r_\chi}(r_\chi|\phi_j)$, $f_{r_\zeta}(r_\zeta|\phi_j)$ and $f_{r_{\chi\zeta}}(r_{\chi\zeta}|\phi_j)$ were parameterized as described in Section II-B with μ and α estimated using a using maximum likelihood procedure [25].

[25] M. DeGroot and M. Schervish, *Probability and Statistics*, 4th ed. Boston, MA: Addison-Wesley, 2012.

REFERENCES

- [1] I. R. Barron, H. S. Yeh, K. Dinesh, and G. Sharma, "Dual modulated QR codes for proximal privacy and security," *IEEE Trans. Image Process.*, vol. 30, pp. 657–669, 2021.
- [2] ISO/IEC, "ISO/IEC 18004:2015: information technology — automatic identification and data capture techniques — QR code bar code symbology specification," Feb. 2015, accessed May 18, 2020. [Online]. Available: <https://www.iso.org/standard/62021.html>
- [3] I. Tkachenko, W. Puech, C. Destruel, O. Strauss, J. Gaudin, and C. Guichard, "Two-level QR code for private message sharing and document authentication," *IEEE Trans. Inf. Forensics Security*, vol. 11, no. 3, pp. 571–583, Mar. 2016.
- [4] G. Chou and R. Wang, "The nested QR code," *IEEE Signal Process. Lett.*, vol. 27, pp. 1230–1234, 2020.
- [5] T. Yuan, Y. Wang, K. Xu, R. R. Martin, and S. Hu, "Two-layer QR codes," *IEEE Trans. Image Process.*, vol. 28, no. 9, pp. 4413–4428, Sep. 2019.
- [6] H.-K. Chu, C.-S. Chang, R.-R. Lee, and N. J. Mitra, "Halftone QR codes," *ACM Trans. Graph.*, vol. 32, no. 6, Nov. 2013.
- [7] G. J. Garateguy, G. R. Arce, D. L. Lau, and O. P. Villarreal, "QR images: Optimized image embedding in QR codes," *IEEE Trans. Image Process.*, vol. 23, no. 7, pp. 2842–2853, Jul. 2014.
- [8] 3GPP, "3GPP TS 38.212 version 15.2.0 Release 15," Jul. 2018, accessed Nov. 16, 2020. [Online]. Available: https://www.etsi.org/deliver/etsi_ts/138200_138299/138212/15.02.00_60/ts_138212v150200p.pdf
- [9] O. Bulan, G. Sharma, and V. Monga, "Orientation modulation for data hiding in clustered-dot halftone prints," *IEEE Trans. Image Process.*, vol. 19, no. 8, pp. 2070–2084, Aug. 2010.
- [10] J. Meriam and L. Kraige, *Engineering Mechanics: Statics*, 7th ed. Hoboken, NJ: Wiley, 2011.
- [11] J. G. Proakis and M. Salehi, *Digital Communications*, 5th ed. New York: McGraw-Hill, 2008.
- [12] J. E. Farrell, P. B. Catrysse, and B. A. Wandell, "Digital camera simulation," *Appl. Opt.*, vol. 51, no. 4, pp. A80–A90, Feb. 2012.
- [13] H. Stark and J. Woods, *Probability, random processes, and estimation theory for engineers*, 2nd ed. Englewood Cliffs, N.J.: Prentice Hall, 1994.
- [14] A. P. Dempster, N. M. Laird, and D. B. Rubin, "Maximum likelihood from incomplete data via the EM algorithm," *J. Roy. Statist. Soc. B (methodol.)*, pp. 1–38, 1977.
- [15] K. Dinesh, J. Lu, S. Dhoro, and G. Sharma, "Channel-wise barcodes for color display applications," *J. Electronic Imaging*, no. 3, pp. 033 021–1 – 18, May/June. 2019.
- [16] "ISETCam," accessed Oct. 19, 2019. [Online]. Available: <https://github.com/ISET/isetcam>
- [17] O. Bulan, V. Monga, G. Sharma, and B. Oztan, "Data embedding in hardcopy images via halftone-dot orientation modulation," in *Proc. SPIE: Security, Forensics, Steganography, and Watermarking of Multimedia Contents X*, vol. 6819, Jan. 2008, pp. 68 190C–1–12.
- [18] K. Niu and K. Chen, "CRC-aided decoding of polar codes," *IEEE Commun. Lett.*, vol. 16, no. 10, pp. 1668–1671, 2012.
- [19] A. Cassagne, O. Hartmann, M. Léonardon, K. He, C. Leroux, R. Tajan, O. Aumage, D. Barthou, T. Tonnellier, V. Pignoly, B. Le Gal, and C. Jégo, "AFF3CT: A fast forward error correction toolbox!" *Elsevier SoftwareX*, vol. 10, p. 100345, Oct. 2019.
- [20] R. Wang and R. Liu, "A novel puncturing scheme for polar codes," *IEEE Commun. Lett.*, vol. 18, no. 12, pp. 2081–2084, 2014.
- [21] "AFF3CT: A fast forward error correction toolbox!" accessed Sept. 23, 2020. [Online]. Available: <https://github.com/aff3ct/aff3ct>
- [22] "Secure password generator," accessed Oct. 17, 2019. [Online]. Available: <https://passwordsgenerator.net/>
- [23] S. Wilson, *Digital Modulation and Coding*. Upper Saddle River, NJ, USA: Prentice Hall, 1996.
- [24] "ZXing C++ port," accessed Oct. 15, 2019. [Online]. Available: <https://github.com/glassechidna/zxing-cpp>

Supplementary Material for “Optimized Modulation and Coding for Dual Modulated QR Codes”

Irving Barron and Gaurav Sharma

S.I. OVERVIEW

This document provides Supplementary Material for the paper [1]. Sections S.II and S.III, respectively, provide details of the derivations of: (a) the semi-major axis a_j for the optimized modulation in Eqn. (3) and (b) the square-root of the normalized analytical area moments of inertia $\sqrt{\tau_{j,k}^\eta/\pi\epsilon(a_j^\eta)^2\Delta^2}$ for an elliptical disk in Eqn. (6).

S.II. SEMI-MAJOR AXIS FOR OPTIMIZED MODULATION

To obtain the expression for the semi-major axis a_j for the optimized modulation in Eqn. (3) of Section II-A, in the 2D orthogonal coordinate system (χ, ζ) , consider the region $(\chi_0 - \Delta/2) \leq \chi \leq (\chi_0 + \Delta/2)$ and $(\zeta_0 - \Delta/2) \leq \zeta \leq (\zeta_0 + \Delta/2)$ corresponding to a square module that constrains an (optimized) elliptical dot rotated by an angle $\phi_j = \pi j/M$, for $j = 0, 1, \dots, (M-1)$, and with semi-major axis a_j oriented at ϕ_j with respect to the χ -coordinate, where (χ_0, ζ_0) denote the coordinates for the center of both the module and the elliptical dot, and Δ the module's length along each axis. The perimeter for the aforementioned elliptical dot can be described parametrically as $f(t) = (\chi(t), \zeta(t))$, $0 \leq t \leq 2\pi$, with,

$$\chi(t) = a_j \cos t \cos \phi_j + (\epsilon a_j) \sin t \sin \phi_j + \chi_0, \quad (\text{S.1})$$

$$\zeta(t) = a_j \cos t \sin \phi_j - (\epsilon a_j) \sin t \cos \phi_j + \zeta_0, \quad (\text{S.2})$$

where (ϵa_j) is the length of the semi-minor axis.

The extrema t^* of (S.1) satisfies

$$-a_j \sin t^* \cos \phi_j + (\epsilon a_j) \cos t^* \sin \phi_j = 0. \quad (\text{S.3})$$

Whence it can be seen that

$$t^* = \arctan(\epsilon \tan \phi_j). \quad (\text{S.4})$$

For optimal modulation, the dot has the largest possible size while being constrained within the module boundaries. For $0 \leq j \leq M/4$ and $3M/4 \leq j \leq (M-1)$, the extremum of (S.1) corresponds to the extent of the square module along the χ -coordinate, i.e.,

$$\chi(t^*) = a_j \cos t^* \cos \phi_j + \epsilon a_j \sin t^* \sin \phi_j + \chi_0 = \Delta/2 + \chi_0. \quad (\text{S.5})$$

Solving for a_j we obtain

$$a_j = \frac{\Delta/2}{\cos t^* \cos \phi_j + \epsilon \sin t^* \sin \phi_j} = \frac{\Delta/2}{\sqrt{\epsilon^2 \sin^2 \phi_j + \cos^2 \phi_j}}. \quad (\text{S.6})$$

For $M/4 < j < 3M/4$, using an analogous argument that the extrema of (S.2) corresponds to the module boundary along the ζ coordinate, we obtain

$$a_j = \frac{\Delta/2}{\sqrt{\epsilon^2 \cos^2 \phi_j + \sin^2 \phi_j}}. \quad (\text{S.7})$$

Equations (S.6) and (S.7), can be combined and written as the single equation

$$\begin{aligned} a_j &= \frac{\Delta/2}{\sqrt{\epsilon^2 \sin^2(\phi_j + \theta_j) + \cos^2(\phi_j + \theta_j)}} \\ &= \frac{\Delta/2}{\sqrt{\epsilon^2 \sin^2\left(\frac{\pi j}{M} + \theta_j\right) + \cos^2\left(\frac{\pi j}{M} + \theta_j\right)}}, \end{aligned} \quad (\text{S.8})$$

where $\theta_j = \pi/2$ for $M/4 < j < 3M/4$ and $\theta_j = 0$ otherwise.

S.III. AREA MOMENT OF INERTIA FOR AN ELLIPTICAL DISK ABOUT A ROTATED AXIS

The analytical area moments of inertia for elliptical disks corresponding to modulated elliptical dots in Eqn. (6) of Section II-A can be obtained in a relatively straightforward fashion using known results in mechanics [2, Appendix A]. For completeness, we provide the derivation here. For the elliptical disk depicted in Fig. S.1 (a), which is centered at the origin with semi-major axis with length a_j^η aligned with the χ -axis and having an eccentricity parameter ϵ , the area moments of inertia about the two orthogonal axes χ and ζ are $\tau_\chi = \frac{\pi}{4} a_j^\eta (\epsilon a_j^\eta)^3$ and $\tau_\zeta = \frac{\pi}{4} (a_j^\eta)^3 (\epsilon a_j^\eta)$, respectively, and the corresponding product of inertia $\tau_{\chi\zeta}$ is zero. For the elliptical disk shown in Fig. S.1 (b) which represents an elliptical dot modulated by counter-clock wise rotation by an angle $\phi_j = \pi j/M$ with respect to its major axis, the area moment of inertia about the purple axis that passes through the origin at an angle $\pi k/M$ can be expressed in terms of τ_χ and τ_ζ , and obtained as [2, Appendix A]

$$\begin{aligned} \tau_{j,k}^\eta &= \frac{\tau_\chi + \tau_\zeta}{2} - \frac{\tau_\chi - \tau_\zeta}{2} \cos 2\psi_{j,k} + \tau_{\chi\zeta} \sin 2\psi_{j,k}, \\ &= \frac{\pi\epsilon (a_j^\eta)^4 (\cos^2 \psi_{j,k} + \epsilon^2 \sin^2 \psi_{j,k})}{4}, \end{aligned} \quad (\text{S.9})$$

where $\psi_{j,k} = \pi(k-j)/M$.

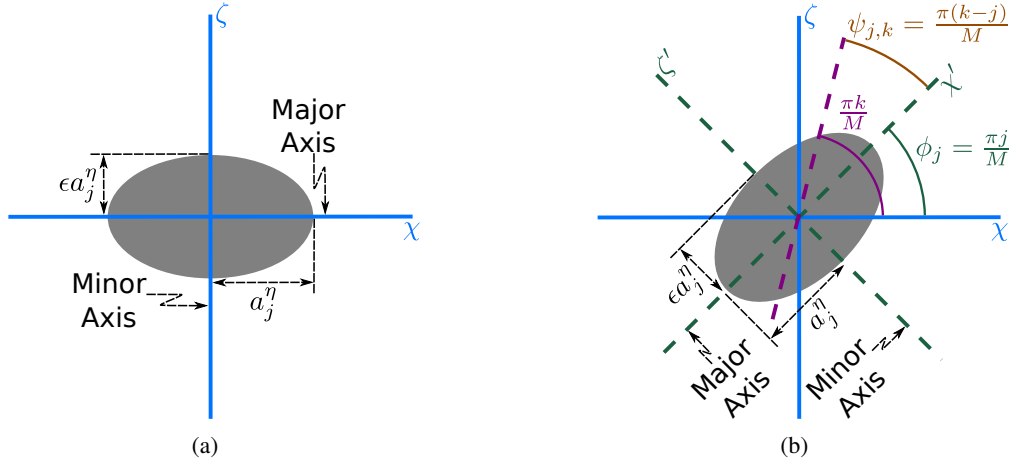


Fig. S.1: Elliptical disk oriented: (a) with major and minor axes aligned with the χ and ζ axes, respectively, (b) at a rotation of $\pi j/M$. The area moment of inertia for the rotated disk in (b) about the axis (shown in purple) through the center that is rotated at an angle $\pi k/M$ is computed in terms of the area moments of inertia for the disk in (a) about the two orthogonal axes χ and ζ .

Dividing by the area of the module and the area of the dot, we obtain a normalized area moment of inertia

$$\frac{\tau_{j,k}^\eta}{\pi\epsilon (a_j^\eta)^2 \Delta^2} = \frac{(a_j^\eta)^2 (\cos^2 \psi_{j,k} + \epsilon^2 \sin^2 \psi_{j,k})}{4\Delta^2}. \quad (\text{S.10})$$

Motivated by the fact that signal space representations commonly used in digital communications use amplitude (rather than power) coordinates, we take a square root to obtain

$$\begin{aligned} \sqrt{\frac{\tau_{j,k}^\eta}{\pi\epsilon (a_j^\eta)^2 \Delta^2}} &= \sqrt{\frac{(a_j^\eta)^2 (\cos^2 \psi_{j,k} + \epsilon^2 \sin^2 \psi_{j,k})}{4\Delta^2}} \\ &= \frac{a_j^\eta}{2\Delta} \sqrt{\cos^2 \psi_{j,k} + \epsilon^2 \sin^2 \psi_{j,k}}. \end{aligned} \quad (\text{S.11})$$

REFERENCES

- [1] I. R. Barron and G. Sharma, "Optimized modulation and coding for dual modulated QR codes," 2022, submitted for review.
- [2] J. Meriam and L. Kraige, *Engineering Mechanics: Statics*, 7th ed. Hoboken, NJ: Wiley, 2011.